Journal of Materials Chemistry A

ROYAL SOCIETY OF CHEMISTRY

PAPER

View Article Online
View Journal | View Issue

Cite this: J. Mater. Chem. A, 2024, 12, 32054

Composite oxide cooling pigments mitigate the impact of urban heat islands†

G. P. Darshan,*[ab] Akshay Arjun,[b] H. B. Premkumar,[b] Elisa Moretti[c] and Alberto Vomiero *[cd]

The escalating threat of ever-increasing urban heat islands presents a significant global challenge regarding energy usage. Hence, the passive daytime solar radiative cooling technique relying on cooling materials is considered an innovative strategy to mitigate this issue without the utilization of any external energy. However, typical solar reflective cooling materials tend to have a bright white appearance, hence prompting an interest in aesthetic-colored reflective coolers with the requisite properties. However, achieving a balance between properties and appearance remains challenging. The present work establishes the synthesis of $La_2W_2O_9$ and $La_2W_{1.86}M_{0.14}O_9$ (M = Co, Cu, Zn, and Fe) radiative cooling pigments showcasing high near-infrared reflectance *via* a solution combustion route. Doping with different ions results in a tunable hue, enabling the preparation of coated surfaces with variable colors. The nano-pigments exhibited a pure triclinic phase of LaW_2O_9 with the *P*1 space group. Doped transition metal chromophores were successfully substituted into the LaW_2O_9 lattice without altering its initial structure. The best performing $La_2W_{1.86}Fe_{0.14}O_9$ cooling nano-pigment exhibits a relatively high near-infrared reflectance of around 97.8% with International Commission on Illumination chroma color coordinates L^* = 62.77, a^* = 19.34, and b^* = 19.79. Interestingly, the thermal conductivity of the prepared pigments was found to be 0.07–0.08 W m^{-1} K^{-1}, which is relatively smaller than conventional roofing materials, implying their advantage in cooling systems. Thanks to the high reflectance and low thermal conductivity of the synthesized pigments, a decrease in the interior temperature was recorded, ranging from 7 to 10 °C under infrared-light illumination for up to 60 minutes. Furthermore, building energy simulation results indicate that 17.54 kW h m^{-2} of electricity can be saved annually if the colored $La_2W_{1.86}Fe_{0.14}O_9$ nano-pigment is employed. The aforementioned results demonstrated the efficacy of the prepared $La_2W_{1.86}M_{0.14}O_9$ (M = Co, Cu, Zn, and Fe) cooling nano-pigments as passive daytime solar radiative cooling materials to mitigate urban heat islands and achieve energy sustainability.

Received 11th June 2024
Accepted 8th October 2024

DOI: 10.1039/d4ta04027a

rsc.li/materials-a

1. Introduction

In recent decades, population migration toward metropolitan areas due to epicenter industrialization has resulted in an increase in population and building density.[1] This high density of population and buildings in urban regions traps solar radiation, resulting in heat issues, namely urban heat islands (UHI), heat pollution, and heatwaves.[1,2] It is predicted that global temperatures could increase by 1.5 °C or more by 2035 compared to pre-industrial levels.[3] In particular, the building (commercial and residential) and industrial sectors are responsible for approximately 95% of global heating.[4] As the planet warms, ensuring sustainable and equitable cooling becomes a primary necessity.[5] Henceforth, cooling technologies play a vital role in improving human life since they support thermal comfort in living areas, prevent heat shock, and extend food preservation. Furthermore, energy consumption for cooling technology has enhanced drastically over the world.[6] According to the International Energy Agency, by 2050 the global energy requirement for cooling technology is projected to increase by 45% as compared to 2016.[7,8] Therefore, developing eco-friendly and efficient cooling strategies to reduce energy consumption, mitigate energy crises, reduce energy costs, cut greenhouse gas emissions and associated heat issues, and support sustainable development has become the subject of current research.[9]

It is widely known that only 5% of solar radiation falls in the ultraviolet (UV) range (300–400 nm), 43% falls in the visible

[a]Physics and Astronomy Department, University of Padova, Via Marzolo 8, Padova I-35131, Italy. E-mail: darshubavimane@gmail.com
[b]Department of Physics, Faculty of Natural Sciences, M. S. Ramaiah University of Applied Sciences, Ramaiah Technical Campus, Bengaluru 560058, India
[c]Department of Molecular Sciences and Nanosystems, Ca' Foscari University of Venice, Via Torino 155, Venezia, 30172, Italy
[d]Division of Materials Science, Department of Engineering Sciences and Mathematics, Luleå University of Technology, Luleå, 97187, Sweden. E-mail: alberto.vomiero@ltu.se

† Electronic supplementary information (ESI) available. See DOI: https://doi.org/10.1039/d4ta04027a

range (400–800 nm), and the remaining 52% is distributed in the near-infrared (NIR) range (800–2500 nm).[10] The maximum heat generation is mainly ascribed to the absorption of near-infrared photons.[11] In view of this, passive cooling materials are considered to be the most efficient method to mitigate heat issues.[12] They have excellent solar reflectivity as well as thermal emissivity, consequently reducing the solar to heat-energy conversion.[13] Hence, NIR-reflecting cooling materials have attracted significant attention from the research community as they are considered to offer a strategic way to achieve long-term effects (*i.e.*, energy conservation is an eco-friendly and sustainable path) and immediate impacts (*i.e.*, a cooler interior even amid high solar irradiance) to alleviate global warming.[14] At present, inorganic pigments with aesthetic properties are gaining interest and are conducive to diminishing UHIs, since they exhibit excellent thermal, environmental, and chemical stability, compared to organic pigments.[15] To date, several inorganic cooling pigments with remarkable NIR reflectance have been reported. For instance, a white-colored titanium dioxide pigment was conventionally used and exhibited NIR reflectance of ~87%, achieving greater chemical stability.[16] Zhou *et al.*[17] studied a series of $Zn_{1-x}A_xWO_4$ (A = Co, Mn, and Fe) cooling pigments with various hues, exhibiting a maximum NIR reflectance of 96.66%. Similarly, bright green Y_2BaCuO_5 pigment (62% reflectance),[18] Ce_2S_3 red pigment (77.09% reflectance),[19] dark orange colored $La_2Ce_2O_7$:Pr^{4+} pigment (72.47% reflectance),[20] and blue Fe^{3+}-doped $YMnO_3$ pigment (60.6% reflectance),[21] *etc.* were also studied. In addition, several NIR reflective pigments and their NIR reflectance is tabulated in Table S1†.[22–31]

Rare-earth (RE) tungstates are very interesting due to its optoelectronic and thermal properties. To date, several categories of RE tungstate-based materials have been studied, namely $RE_6W_2O_{15}$, $RE_2W_2O_9$, RE_2WO_6, $RE_2W_3O_{12}$, RE_6WO_{12}, *etc.*[32,33] Several reports are available on $La_2Mo_2O_9$ (LAMOX),[34] but lanthanum tungstate $La_2W_2O_9$ has not been studied in detail so far. $La_2W_2O_9$ has excellent optical absorption in the visible region (the main cause of coloration), resulting from optically active tungstate ligand field effects around the transition metal ions.[35] In addition, charge transfer among two atoms in a host was considered a factor for coloration. Generally, the cause of color in inorganic solids arises from a variety of physical and chemical mechanisms. There are mainly three types of electronic transitions that can be used to explain the color in inorganic color pigments, *i.e.*, (i) crystal field or d–d transitions in transition metal oxides, (ii) charge transfer transitions in compounds with multi-centered ions, and (iii) valence band to conduction band transitions in semiconductors. Generally, charge transfer transition can be of three different types: (i) metal-to-metal charge transfer, (ii) ligand-to-metal charge transfer, and (iii) metal-to-ligand charge transfer.[36] Metal-to-metal charge transfer can occur when two atoms are close to one another (*i.e.* transition metal ions in coordination sites sharing edges or faces) and the energy required to transfer an electron from one atom to another within these compounds has been found to correspond to the energies of the visible light. The intervalence charge transfer occurs due to a momentary change of valences when an electron is transferred between two neighboring cations in adjacent coordination sites.[37] Notably, $La_2W_2O_9$ material exhibits asymmetric triclinic geometry and W^{4+} (ionic radius of 0.66 Å with VI coordination) can be conceivably replaced by transition metals, which may result in the formation of various colors. To date, the synthesis of transition metals doped triclinic structured $La_2W_2O_9$ pigments with various hues *via* the solution combustion (SC) route to achieve high NIR reflectance has not been reported yet.

In the present work, we have focused on the synthesis of various colored $La_2W_2O_9$ and $La_2W_{1.86}M_{0.14}O_9$ (M = Co, Cu, Zn, and Fe) cooling nano-pigments *via* a self-ignition SC method to develop high NIR reflectance with excellent photo, chemical, and thermal stability. The phase purity and structure of the prepared pigments were investigated in detail. The optical properties of the nano-pigments in the UV-vis-NIR range are discussed in depth. The colorimetric parameters (in the $L^*a^*b^*$ color space) were explored experimentally. In addition, the chemical valence state of the synthesized nano-pigment was also assessed by X-ray photoelectron spectroscopy (XPS) analysis. Finally, the chemical, thermal, photostability, and thermal conductivity of the pigments were also tested and discussed in detail relating to cooling applications. Moreover, the energy consumption analysis of the building coated with the synthesized pigment was simulated by *EnergyPlus* software compared with the cement exterior wall to endorse the advantage of the application of the pigment layer with energy-saving ability.

2. Experimental

2.1. Materials

The lanthanum(III) nitrate hexahydrate [($La(NO_3)_3 \cdot 6H_2O$), 99.99%], tungsten(VI) oxide [(WO_3); 99.99%], cobalt(II) nitrate hexahydrate [($Co(NO_3)_2 \cdot 6H_2O$), 99.99%], copper(II) nitrate trihydrate [($Cu(NO_3)_2 \cdot 3H_2O$), 99%], zinc nitrate hexahydrate [($Zn(NO_3)_2 \cdot 6H_2O$), 99%], and ferric(III) nitrate nonahydrate [($Fe(NO_3)_3 \cdot 9H_2O$), 98%] were purchased from Sigma-Aldrich Com. and employed without any further purification. The laboratory-prepared oxalyl dihydrazide (ODH, $C_2H_6N_4O_2$) was used as a fuel. Nitric acid (HNO_3), hydrochloric acid (HCl), and sodium hydroxide (NaOH) were used in the chemical stability test. A transparent synthetic varnish procured from Asian Paints Ltd. was utilized for coating applications.

2.2. Synthesis of inorganic $La_2W_2O_9$ and $La_2W_{1.86}M_{0.14}O_9$ (M = Co, Cu, Zn, and Fe) nano-pigments

The inorganic cooling $La_2W_2O_9$ and $La_2W_{1.86}M_{0.14}O_9$ (M = Co, Cu, Zn, and Fe) nano-pigments were synthesized *via* the SC route. Initially, an appropriate amount of WO_3 was taken in a Petri dish and well-dissolved in an aqueous NH_4OH solution using a bath sonicator for 30 min. Then, the obtained reaction mixture was constantly stirred using a magnetic stirrer for 30 min maintained at temperature of 90 °C, resulting in the ammonium tungstate solution. Later, the stoichiometric quantities of $La(NO_3)_3$, $Co(NO_3)_2$, and ODH were added to the formerly prepared solution and well-dissolved in double

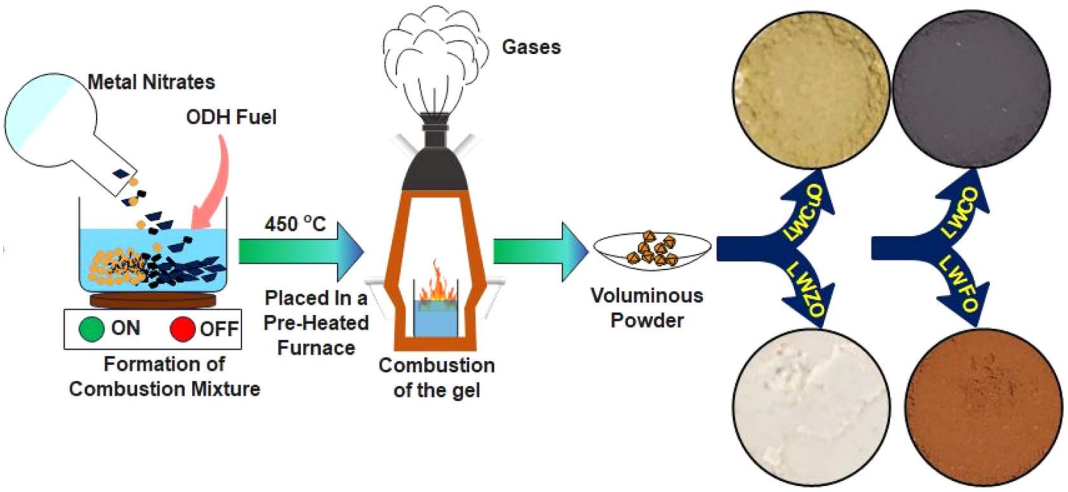

Fig. 1 A schematic representation demonstrating the synthesis process of nano-pigments *via* the SC method.

distilled water (100 mL) using a magnetic stirrer maintained at 450 rpm for 10 min to obtain a homogeneous solution. Then, the Petri-dish-containing reaction mixture was placed in a pre-heated muffle furnace maintained at 450 ± 10 °C. The mixture endured thermal dehydration resulting in a viscous gel. Within a short period, the viscous gel self-ignited inside the mixture, and subsequently exothermic combustion took place with an intense flame accompanied by the liberation of a significant amount of N_2 and CO_2 gases, which resulted in a fluffy-textured voluminous solid. The voluminous solid was finely ground using a mortar and pestle, subsequently transferred to aluminum crucibles, and placed in a muffle furnace for calcination at a temperature of 1000 °C for 6 h. Fig. 1 depicts a schematic representation demonstrating the synthesis of nano-pigments *via* the SC method. The whole synthesis procedure was repeated by using different dopants (Cu, Zn, and Fe) by following the above protocol. Herein, the prepared $La_2W_2O_9$, $La_2W_{1.86}Co_{0.14}O_9$, $La_2W_{1.86}Cu_{0.14}O_9$, $La_2W_{1.86}Zn_{0.14}O_9$, and $La_2W_{1.86}Fe_{0.14}O_9$ nano-pigments are abbreviated to LWO, LWCO, LWCuO, LWZO, and LWFO, respectively.

2.3. Preparation of the coating using a synthesized nano-pigment and its passive daytime radiative cooling application

The best-performing LWFO nano-pigment was selected for NIR-reflecting coating over aluminum sheets. The procedure to create the nano-pigment coating is as follows; the optimized LWFO nano-pigment was well mixed with synthetic varnish in the weight ratio of 1 : 1 by inserting a titanium horn (6 mm diameter) ultrasound probe sonicator maintained at 22 kW for 1 h to ensure uniform dispersion of the nano-pigment in the varnish binder. The obtained emulsion was uniformly coated onto an aluminum sheet using a paintbrush and allowed to dry at room temperature. Later, the coated aluminum sheets were subjected to thermal shielding analysis. The thermal shielding effect of the coated aluminum sheets was examined by designing an experimental setup. The system comprises two plywood house models (8 × 8 × 8 cm^3) with pigment-coated aluminum sheet roofing (10 × 10 cm^2). A narrow hole was provided just 2 cm below the roof to facilitate measuring temperature. The whole system was then subjected to illumination under IR lamps. Simultaneously, the temperatures were recorded every 5 minutes. The pictorial diagram illustrating the preparation of coating using a synthesized nano-pigment and its passive daytime radiative cooling application is shown in Fig. 2.

2.4. Characterization

Powdered X-ray diffraction (PXRD) studies of the prepared nano-pigments were conducted using a Rigaku SmartLab diffractometer with a monochromatic CuKα_1 (1.541 Å) source. The divergence slit, scatter slit, and receiving slit were set at 1°, 1°, and 0.3 mm, respectively. Data was recorded in the scan range 10°–80° using the continuous scan mode, with a scan speed of 4° min^{-1} and a sampling pitch of 0.02°. The lattice parameters and reliability factors of the pigments were estimated by the Rietveld refinement method using the *Fullprof* suite program.

A Tescan Vega 3 scanning electron microscope (SEM) equipped with a tungsten-heated cathode electron gun with a resolution of 3.0 nm at 30 kV and maximum field of view of 0.08 μm was used to analyze the surface morphology of the synthesized cooling pigments. The SEM instrument was also equipped with TESCAN Essence™ energy-dispersive X-ray spectroscopy (EDX), which is utilized for elemental composition analysis of the pigments.

Fourier transform infrared spectroscopy (FTIR) analysis was carried out using a Bruker Alpha II FTIR spectrometer with a diamond crystal attenuated total reflection (ATR) accessory to identify chemical bonds/functional groups present in the prepared nano-pigments.

XPS analysis of the selected nano-pigment was performed using a Physical Electronics (PHI 5000 VersaProbe III) instrument equipped with a micro-focused monochromatic X-ray beam and a C60 ion gun. All acquitted binding energies were referenced to the C 1s peak (283.7 eV) arising from adventitious carbon.

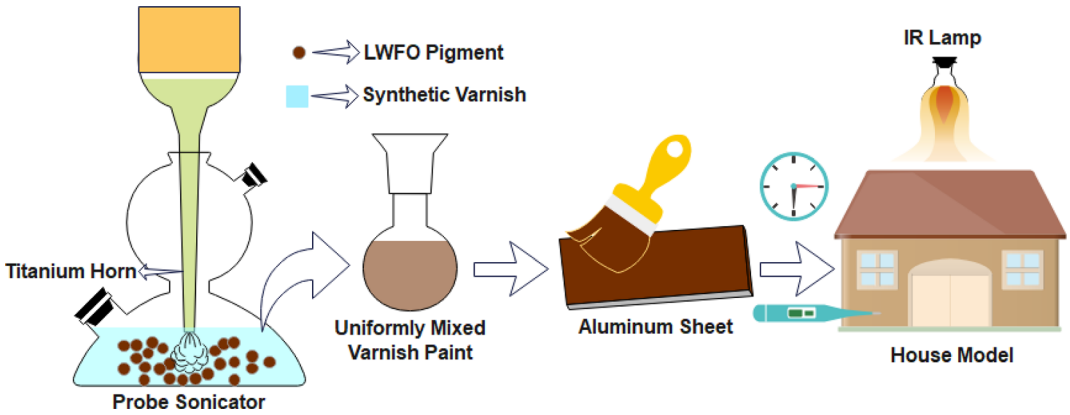

Fig. 2 A pictorial diagram illustrating the preparation of a coating using a synthesized nano-pigment and its passive daytime radiative cooling applications.

Thermal conductivity measurements of the synthesized cooling pigments were performed using a TCi thermal conductivity analyzer system (C-Therm Technologies Ltd), which offers a thermal conductivity range of 0 to 500 W m^{-1} K^{-1} and a thermal effusivity range of 5 to 40 000 W $s^{\frac{1}{2}}$ m^{-2} K^{-1}.

A PerkinElmer (Lambda 750) spectrophotometer maintained at a slit width of 0.5 nm was used to study the diffuse reflectance performance of the prepared pigments in the range of 200 nm to 2600 nm.

A Bruker Vertex 70v with a gold mirror as a reference was used for IR emissivity measurements in the 1.25–28.25 μm wavelength range.

The chromatic characteristics *i.e.*, CIE 1976 $L^*a^*b^*$ color scheme of the pigments were recorded using a Datacolor® 800 benchtop dual beam $d/8°$ spectrophotometer. The spectrophotometer is equipped with an integrating sphere of 152 mm and utilizes a pulsed xenon light source filtered to D65. Herein, L^* specifies the lightness scale in a range from 0 (black) to 100 (white). The a^* coordinate represents the green (−ve) to red (+ve) transition, whereas the blue (−ve) to yellow (+ve) transition is denoted by b^*. Chroma (c^*) gives the saturation of color and is estimated using the following equation:[38]

$$C^* = [(a^*)^2 + (b^*)^2]^{1/2} \quad (1)$$

Another factor, the hue angle ($h°$ in degrees) was characterized and ranges from 1 to 360°. The $h°$ value was calculated using the given equation:[38]

$$h^\circ = \tan^{-1}(b^*/a^*) \quad (2)$$

In addition, the ASTM standard number G173-03 was adopted to measure solar reflectance data.[39] The solar reflectance of the prepared nano-pigments was elucidated in the range of 700–2500 nm using the given equation:[40]

$$R^* = \frac{\int_{700}^{2500} r(\lambda) i(\lambda) \mathrm{d}\lambda}{\int_{700}^{2500} i(\lambda) \mathrm{d}\lambda} \quad (3)$$

here, $r(\lambda)$ is the experimentally derived spectral reflectance data of the pigments, and $i(\lambda)$ is the standard solar spectral irradiance as per the ASTM standard model G173-03 (in W m^{-2} mm^{-1}). For daytime radiative cooling analysis and photostability test, a Philips BR125 IR 250 W bulb was used. A photostability test of the pigments was performed by irradiating a light source from ~15 cm from a top in a closed chamber.

The surface roughness of the nano-pigment-coated aluminum sheet was examined using a Bruker (DektakXT) surface stylus profilometer with a stylus radius of 2 microns. The wettability studies *i.e.*, water contact angle (WCA) measurements were performed by employing a Kyowa (DM501) contact angle meter *via* sessile drop mode.

3. Results and discussion

PXRD patterns of the prepared LWO, LWCO, LWCuO, LWZO, and LWFO nano-pigments are depicted in Fig. 3(a). The characteristic patterns of the synthesized nano-pigments are well in accordance with the standard pattern of LWO with the triclinic phase and the $P1$ space group. No impurities/spurious peaks are present in the PXRD profiles, which indicates that the doped chromophores have been successfully incorporated into the LWO lattice without generating any other secondary phases. In addition, the effective doping was further validated *via* the EDX spectrum (Fig. S1†). The spectrum revealed minor peaks corresponding to dopants Co (L), Cu (L), Zn (L), and Fe (L) without any traces of impurity. The acceptable ionic radius percentage difference (Δ_r) between the host cation and dopant ions in the synthesized nano-pigments was estimated using the following equation:[41]

$$\Delta_r = \frac{R_h(\mathrm{CN}) - R_d(\mathrm{CN})}{R_h(\mathrm{CN})} \times 100\% \quad (4)$$

where, CN is the coordination number, and R_h and R_d are the ionic radii of host cation and dopant ions, respectively. In the present work, by considering the R_h and R_d values of the W^{4+} cation (0.66 Å) and dopant ions (Co is 0.53 Å; Cu is 0.54 Å; Zn is 0.74 Å; Fe is 0.61 Å) with VI coordination, the $\Delta_{r(W-Co)}$, $\Delta_{r(W-Cu)}$, $\Delta_{r(W-Zn)}$, and $\Delta_{r(W-Fe)}$ values were estimated and obtained to be 19.69%, 18.18%, 12.12%, and 7.57%, respectively. The estimated Δ_r values were found to be less than 30% (*i.e.*, maximum

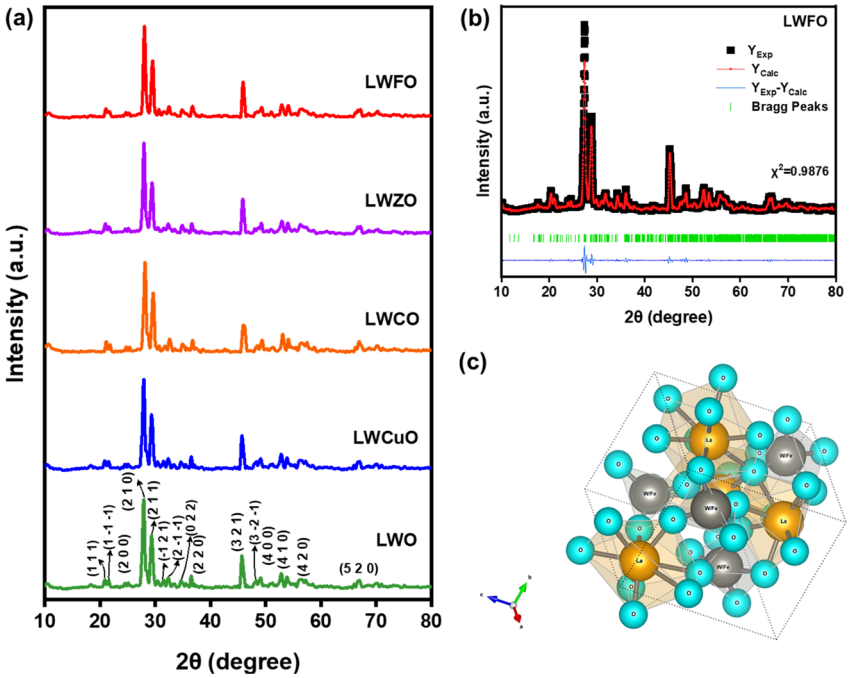

Fig. 3 (a) PXRD profiles of the synthesized cooling pigments, (b) Rietveld refinement, and (c) a packing diagram of the LWFO nano-pigment.

acceptable range), which indicated that the dopant ions successfully occupied the W^{4+} site in the LWO lattice. The average crystallite size (D) of the synthesized nano-pigments was calculated using Scherrer's relation.[42] The estimated D values of the nano-pigments were found to be in the range of 23–30 nm (Table S2†). In addition, the Rietveld refinement analysis of the best-performing LWFO nano-pigment was carried out to investigate its crystal structure and the changes occurring in the lattice owing to the doping chromophore.[43] Fig. 3(b) shows the experimental, refined, and difference profiles attained after the refinement of the LWFO nano-pigment. Following the detailed refinement analysis, it was observed that the synthesized nano-pigment was well crystallized in the triclinic structure with space group $P1$ and showcase lattice parameters $a = 7.2823$ Å, $b = 7.2984$ Å, $c = 7.4285$ Å, $\alpha = 90.23°$, $\beta = 89.88°$, $\gamma = 87.23°$, and $V = 393.95$ Å^3. As shown in the figure, there was a clear agreement between the experimental and calculated profiles. The reliability factor (*i.e.*, goodness of fit (χ^2)) of the fitted plots was found to be 0.9876, demonstrating the best fitting between experimental and refined profiles. Furthermore, lattice parameters were used to model the crystal structure of LWFO nano-pigment *via* the *VESTA* program. Fig. 3(c) shows the crystal structure of the prepared LWFO nano-pigment. The structure of the triclinic LWFO pigment has isolated $[W_4O_{18}]^{-12}$ groups alternating with trigonal bipyramids resulting in a three-dimensional framework with La atoms in both 9- and 10-fold oxygen polyhedral.[44]

SEM images of the prepared LWCO, LWCuO, LWZO, and LWFO nano-pigments are depicted in Fig. 4. The LWCO nano-pigments revealed an irregularly stacked ribbon-like morphology (Fig. 4(a)). Following close inspection, an agglomerated rod-like structure of the synthesized LWCuO nano-pigment was observed (Fig. 4(b)). LWZO nano-pigments exhibit irregularly shaped structures (Fig. 4(c)). Interestingly, LWFO nano-pigments showcase a flaky-type structure with an irregular stacking morphology with voids (Fig. 4(d)). The observed morphologies of the synthesized nano-pigments are obvious in the SC-derived samples, which are ascribed to local sintering by the generation of high temperatures during the combustion in the system.[45] Notably, the observed voids showed excellent reflectance performance *via* efficient sunlight scattering. Herein, the product's morphology can be greatly influenced by the two important physical parameters, including reaction temperature and the amount of gas released. Normally, temperature accelerates reactions, grain growth, and sintering results in agglomeration and crystallinity. However, gaseous products during the combustion process make solid materials fluffy and voluminous, which leads to higher porosity of the products. However, the temperature and amount of gas released depend on various experimental conditions. Among them are the precursors, composition of the precursors, fuel, fuel-to-oxidizer ratio, methods of heating, and ignition of the initial solutions, *etc.*[46,47] In the present work, fuel-to-oxidizer ratios and fuel during synthesis are maintained constantly throughout the experiments; though change in the morphology of the products was noticed. However, we believe that different dopants used (even when maintaining constant concentration) in the preparation might be responsible for variations in the morphology of the pigments. The EDX spectrum of the selected portions of the synthesized LWCO, LWCuO, LWZO, and LWFO nano-pigments is shown in Fig. S1.† The spectrum revealed prominent characteristic X-ray peaks located at 0.5, 1.7, and 4.9 keV, which are related to O (K), W (L), and La (K) emissions, respectively.

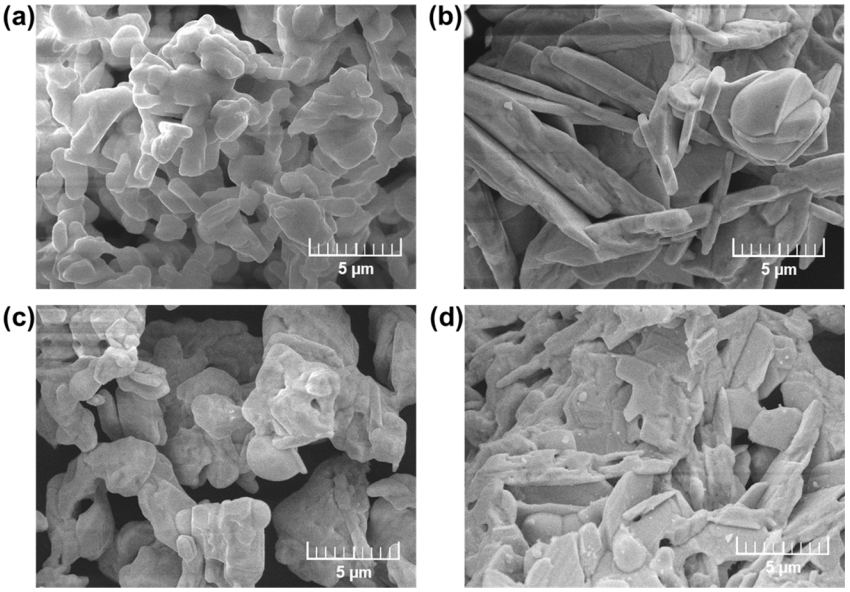

Fig. 4 SEM images of (a) LWCO, (b) LWCuO, (c) LWZO, and (d) LWFO nano-pigments.

Furthermore, minor peaks corresponding to Co (L), Cu (L), Zn (L), and Fe (L) are also identified in the spectrum without any traces of impurity. The quantitative analysis of the constituent elements in the prepared nano-pigments using the EDX spectrum is tabulated in the inset of Fig. S1.† The established results confirmed the appropriate incorporation of chromophores in the host lattice.

The typical XPS-wide survey scan was performed to confirm the elemental state and chemical compositions, the best performing LWFO nano-pigment was chosen and the corresponding survey scan was given in Fig. S2.† The survey scan consists of La 3d, W 4f, Fe 2p, and O 1s core levels, confirming the chemical composition obtained through EDX. The survey exhibits a peak at ~283.7 eV corresponding to C 1s, which is mainly attributed to atmospheric exposure during sample synthesis.[48] To elucidate the chemical state of the individual constituent in the pigment, narrow scan XPS measurements were explored (Fig. 5(a–d)). As can be seen from the high-resolution La 3d scan, there are distinctive two-orbit doublets at 834.27 eV and 850.97 eV, which correspond to the La $3d_{5/2}$ and La $3d_{3/2}$ levels, whereas two shoulder peaks are also clearly noticed at a binding energy equal to 838.03 eV and 855.08 eV (Fig. 5(a)).[49] The obtained results endorse the presence of the La^{3+} state. Furthermore, three significant peaks were positioned at ~31.87 eV, 34.89 eV, and 37.26 eV owing to the W^{4+} state of W $4f_{7/2}$, W $4f_{5/2}$, and W $5p_3$, respectively (Fig. 5(b)).[50] The Fe 2p spectrum (Fig. 5(c)) confirms the existence of Fe $2p_{1/2}$ (709.63 eV) and Fe $2p_{3/2}$ (722.14 eV) levels. In addition, there are two satellite peaks at 701.82 eV and 731.28 eV, indicating the existence of the Fe^{2+} ion (Fig. 5(c)).[51] The survey spectrum of the O 1s witnessed a major peak at 529.57 eV, which is ascribed to the lattice oxygen. Furthermore, surface adsorption of the oxygen or hydroxyl group prompted a small noticeable peak at 527.02 eV (Fig. 5(d)).[41] UV-vis diffuse reflectance (DR) spectra of the prepared nano-pigments spanning in the region 200–2600 nm are shown in Fig. 6(a). The spectra revealed that the synthesized pristine LWO and LWZO nano-pigments did not exhibit any representative absorption in the visible region, hence resulting in a white appearance. Interestingly, the LWFO nano-pigment exhibits strong absorption spanning in the range from 320 to 560 nm. In the LWFO nano-pigment, a deep absorption band centered at 350 nm can be mainly attributed to the $^6A_1(^6S) \rightarrow {}^4E(^4D)$ transition.[52] Further, the absorption band around 510–560 nm is ascribed to the $^6A_1(^6S) \rightarrow {}^4E(^4G)$, and $^6A_1(^6S) \rightarrow {}^4A_1(^4G)$ transitions.[53] In addition, the LWFO pigment shows a significant reduction in reflectance around 700 and 900 nm, which results from $^6A_1(^6S) \rightarrow {}^4T_2(^4G)$ and $^6A_1(^6S) \rightarrow {}^4T_1(^4G)$ bands.[54,55] Here, the d–d transitions of the Fe^{2+} ions are spin-forbidden and Fe^{2+} holds five electrons in the d-orbit, the charge transfer from the partially filled Fe 2d orbit to the empty W 5d orbit leads to a broad UV absorption.[56,57] The LWCuO pigment showcases a maximum reflectance hump between 400 and 800 nm, which is due to the d–d electronic transition of Cu^{2+} ions.[58] However, LWCO nano-pigments exhibit a strong absorption band at around 370–510 nm mainly due to $^4T_{1g} \rightarrow {}^4T_{1g}(P)$ d-electronic of Co^{4+} transition in the LWO system.[59] In addition, the strong peaks at 590 and 730 nm are mainly attributed to the $^4T_{1g} \rightarrow {}^4A_{2g}$ transition.[59] The combination of metal-to-metal charge transfer and d–d transitions of Co^{4+} ions contribute to several hues. Interestingly, strategic doping of the chromophores results in low reflectance in the 300–800 nm region, resulting in different hues of the pigments. Furthermore, the optical energy band gap (E_g) of the synthesized nano-pigments was evaluated using the Kubelka–Munk (K–M) theory. Generally, the K–M function relates the DR of the materials (R) to the scattering coefficient (S) as well as the absorption coefficient (K), as given below:[60]

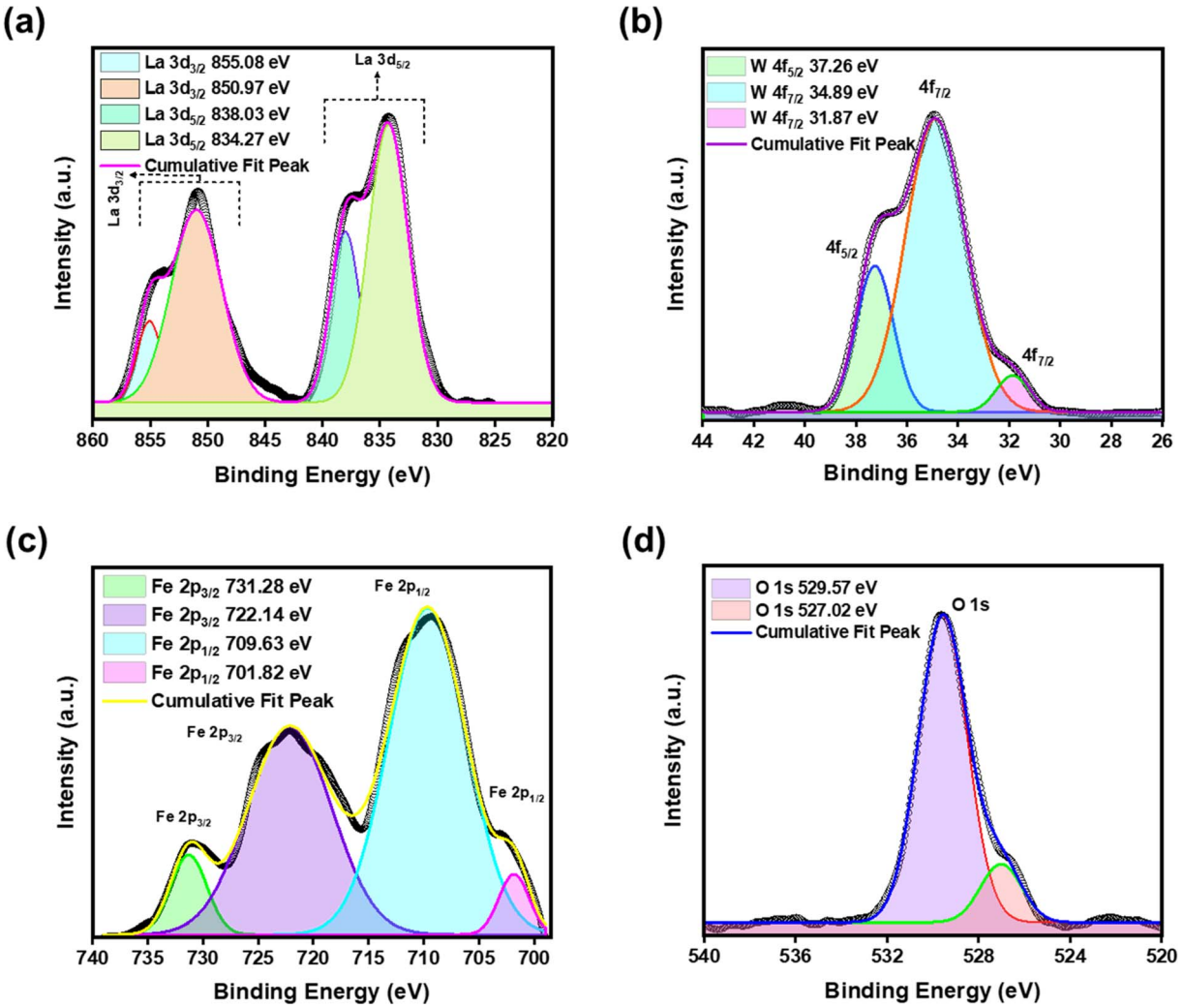

Fig. 5 The XPS binding energy-resolved high-resolution spectrum of LWFO, including (a) La 3d, (b) W 4f, (c) Fe 2p, and (d) O 1s.

$$F(R_\infty) = \frac{(1-R_\infty)^2}{2R_\infty} = \frac{K}{S} \quad (5)$$

In addition, the linear absorption coefficient (α) of a system and the E_g are associated *via* known the Tauc's relation, as follows:[57]

$$\alpha = \frac{A(hv - E_g)^{n/2}}{hv} \quad (6)$$

here, A is a proportionality constant and hv represents photon energy. When the system diffusely undergoes perfect scattering, α is equal to 2. By considering S as a constant, eqn (5) and (6) can be expressed as:[57]

$$[F(R_\infty)hv]^2 = C(hv - E_g)^n \quad (7)$$

where, the value of n *i.e.*, 1, 2, 3, 4, and 6 represents the kind of transitions, such as direct allowed transitions, non-metallic materials, direct forbidden, indirect allowed, and indirect forbidden transitions, respectively.[58] In the present work, the best fitting of eqn (7) ($n = 1$) was obtained for $[F(R_\infty)hv]^2$ *versus* hv, signifying that the band transitions were direct allowed transitions. Fig. 6(b) shows the E_g plots of the prepared nano-pigments. The E_g values were extracted by extrapolating the linear fitted regions to $[F(R_\infty)hv]^2 = 0$. From close inspection, the E_g values of the prepared pristine and nano-pigments were obtained to be around 2.83–3.78 eV (Table S2†). Fig. S3† showcases the FTIR spectra of the prepared pigments. The spectra consisting of a band in the range ~526–684 cm^{-1} was assigned to W–O stretching.[59] However, peaks at ~743 and 801 cm^{-1} were mainly due to C–H bending vibrations, whereas a W–O–W stretching peak at 896 cm^{-1} was noticeable.[60]

To evaluate the energy-saving applications of the synthesized nano-pigments, a detailed study of the NIR reflectance property is imperative. Herein, the NIR reflectance spectra of the synthesized pigments were displayed in Fig. 6(a). The spectra of the LWO material exhibit a maximum peak reflectance of ~90%. Interestingly, after the successful incorporation of the chromospheres in the LWO lattice, the spectra revealed that the maximum peak reflectance was enhanced especially in LWFO nano-pigment (~97.8%) with an average NRI reflectance of 91%. The studied LWO compound shows the optical absorption

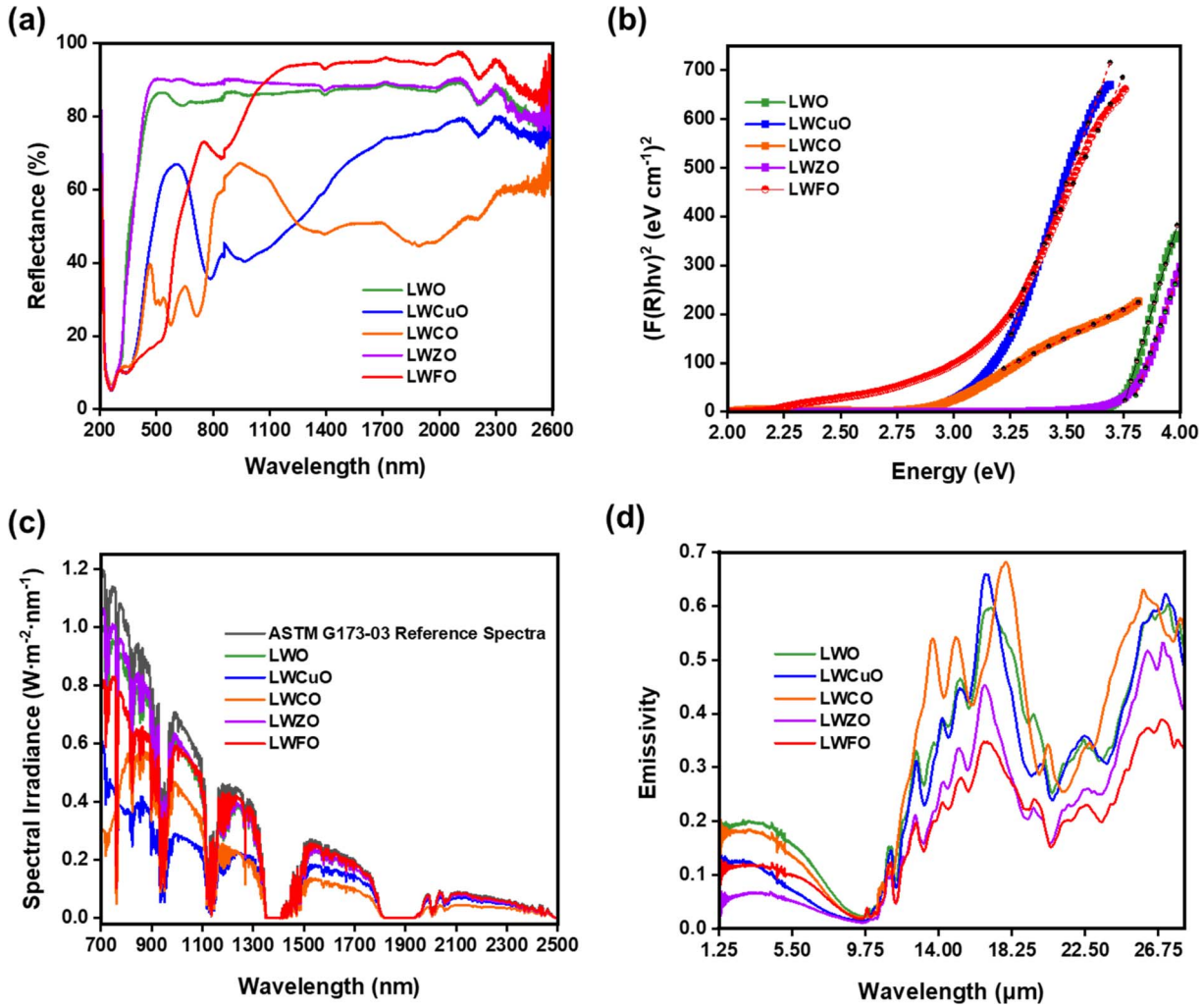

Fig. 6 (a) Reflectance spectra of the prepared cooling pigments in the range of 200–2600 nm, (b) The corresponding energy band gap plots of the nano-pigments, (c) the solar reflectance spectra of the synthesized nano-pigments, and (d) spectral IR emissivity curves of the prepared pigments.

between the valence band (VB) composed of La 5d and O 2p orbitals and the conduction band (CB) composed of W 4d orbital. When Fe^{2+} ions are substituted into the W-ions site, the CB bottom potential level decreases due to Fe 4s orbitals contributing to the CB. As a result, the bandgap of the LWFO pigment is decreased compared to that of LWO (shown in Fig. S4†), thus changing the material's color, which inherently improves the reflectance property of the material. With close inspection of the spectra, the LWZO nano-pigment demonstrated a similar trend by following the LWFO pigment with a reflectance of ~91%. Interestingly, the LWCuO nano-pigment revealed a maximum peak reflectance of 80.07%. Among the synthesized nano-pigments, a lower NIR reflectance was noticed in the LWCO nano-pigment (*i.e.*, ~67%); all the prepared nano-pigments still possess a significantly higher NIR reflectance compared with the previously reported pigments, namely $TiZn_{1.8}Cu_{0.2}O_4$ pigment (R = 62.83%), $TiZn_{1.8}Fe_{0.2}O_4$ (R = 87.81%),[61] $NiAl_2O_4$ pigment (R = 53.0%),[62] Fe_2O_3/TiO_2 composite pigment (R = 68.2%),[63] and $NaFeTiO_4$ pigment (R = 81.43%).[64] In addition, the NIR reflectance property of the pigments is also mainly ascribed to local surface plasmon resonance (LSPR).[65] LSPR of materials is sensitive to the morphology, particle size, and free carrier density. LSPR-induced reflection or absorption is enhanced by the high aspect ratio of nanomaterials.[66] In the present work, the prepared flaky-type LWFO pigment exhibits a higher aspect ratio (due to the LSPR of both the longitudinal plasmon band as well as the transverse plasmon band) than that of LWCO, LWCuO, and LWZO pigments. Therefore, the LWFO pigment showcases excellent NIR reflectance property compared to other pigments. The obtained results demonstrate the significance of the prepared pigments to effectively reflect the maximum part of the solar radiation. Interestingly, these results demonstrate that strategic doping of the appropriate chromophores to tune the hue of the samples with improved IR reflectance is highly significant. Subsequently, the solar reflectance of the pigments was also studied (Fig. 6(c)). The spectra showcase a noticeable quantity of solar irradiance spectral concealment, which

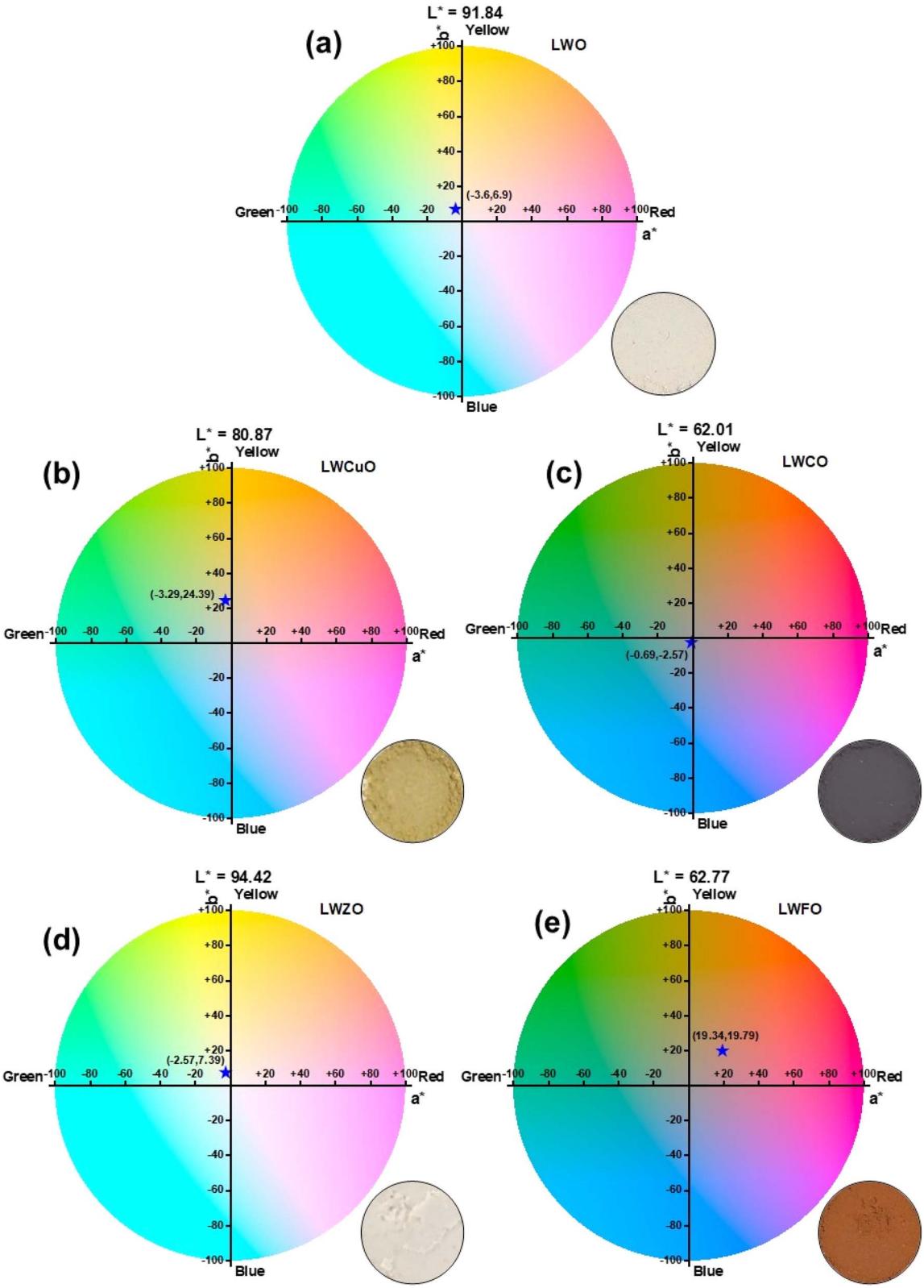

Fig. 7 CIE 1976 *L*a*b* diagrams and related photographic images of the prepared nano-pigments.

indicates that the pigments can be utilized in coatings to reflect heat and that they show promise as cooling nanomaterials for energy saving. Fig. 6(d) shows the IR emissivity curves of the prepared nano-pigments. It can be seen from the figure that the intensive spectral IR emissivity of LWFO is found to be ~0.32 in the 9.75–28.25 μm band and 0.12 in the 1.25–9.75 μm band,

Table 1 The CIE chroma coordinates ($L^*a^*b^*$), chroma (c^*), and hue angle ($h°$) values of the prepared nano pigments compared with corresponding standard colors

	CIE coordinates ($L^*a^*b^*$)							
Pigments	L^*	a^*	b^*	ΔE^*	Chroma (c^*)	Hue angle ($h°$)	Color	Analysis
LWFO	62.77	19.34	19.79	—	27.67	45.66		
Terrazzo Tan	62.02	18.79	20.25	1.264	28	47		Close but distinguishable
Copper trail	62.45	20.44	18.11	4.352	27	42		Slightly different
LWCuO	80.87	−3.29	24.39	—	24.61	97.67		
Pantone C	82.18	−3.5	24.07	1.454	24	98		Close but distinguishable
Soft green	81.01	−3.42	21.22	10.205	21	99		Different
LWCO	62.01	−0.69	−2.57	—	2.66	254.9		
Cool Grey 8 U	61.49	−0.11	−2.17	0.98	2	267		Distinguishable to the practiced eye
Steely gray	61.98	−2.01	−3.03	1.984	4	236		Close but distinguishable
LWZO	94.42	−2.57	7.39	—	7.83	109.2		
Sail cloth/washing line	94.47	−2.04	7.76	0.467	8	105		Distinguishable to the practiced eye
Mental note	93.46	−3.46	7.29	1.762	8	115		Close but distinguishable

which is mainly ascribed to the extremely weak absorption of the pigment. Moreover, the lower spectral emissivity of the pigment was witnessed as the reflectance of the pigment was high. This phenomenon is mainly attributed to pigments having a certain absorption capability in these wavelength bands, which is not strong in other wavelength bands.[67] However, maximum emissivity (*i.e.*, ∼0.68) is witnessed in the LWCO nano-pigment due to the significant absorption of incident light. The CIE 1976 L^*a^*b color coordinates were evaluated to assess the chromatic properties of the synthesized pigments. Fig. 7 shows the CIE L^*a^*b diagrams and photographic images of the LWO, LWCO, LWCuO, LWZO, and LWFO nano-pigments. As shown in the figure, the undoped LWO material exhibits a maximum L^* value of 91.84 with $a^* = -3.6$ and $b^* = 6.9$ (Fig. 7(a)). The LWCuO nano-pigment demonstrates a decrease of the L^* value from 91.84 to 80.87 (Fig. 7(b)), which is ascribed to the effective substitution of the chromophore ions in the LWO lattice site. Interestingly, the value of a^* (−3.29) is almost consistent with the LWO system, nevertheless the b^* value (24.39) shifted towards the yellow side; it is a clear indication that the prepared pigment turned into a near Pantone C-type color (as shown in Table 1) by human visual inspection. CIE

L^*a^*b diagrams of the LWCO and LWFO nano-pigments demonstrate lower L^* values of 62.01 and 62.77, respectively (Fig. 7(c and e)). Among them, the LWCO pigment exhibits $a^* = -0.69$ and $b^* = -2.57$, indicating that the pigment turns a pale grey color, which is only distinguishable by the practiced eye compared with the standard Natural slate (Table 1). The CIE (a^* and b^*) color coordinates of the LWFO nano-pigment are located in the red-yellow degree (19.34 and 19.79) region of the CIE diagram and are close but distinguishable with standard Terrazzo Tan color ($L^* = 62.02$, $a^* = 18.79$, $b^* = 20.25$, and $c^* = 28$). The obtained result demonstrated that the prepared pigment has a nearly tan color perception (inset photo). Under close inspection, the LWZO nano-pigment shows a brilliant white L^* value of 94.42, whereas a^* and b^* values span in the green-yellow degree (Fig. 7(d)), manifesting a close resemblance to the appearance of sail cloth (Table 1). In addition, the color difference (ΔE^*) between the synthesized nano-pigments and commercial pigments was estimated using the following relation:[68,69]

$$\Delta E^* = \sqrt{(\Delta L^*)^2 + (\Delta a^*)^2 + (\Delta b^*)^2} \quad (8)$$

The estimated ΔE^* values of the prepared pigments were tabulated in Table 1. As evident from the table, ΔE^* values of the LWFO pigment are found to be reasonably minimal as compared to other pigments. The obtained result demonstrated that the prepared LWFO pigment can be considered as an alternative solution benefiting from high NIR reflectance properties and a lowest ΔE^* value to replace conventional pigments. Furthermore, C^* and H° values of the LWCO, LWCuO, LWZO, and LWFO nano-pigments are also estimated and tabulated in Table 1.

The stability assessment of the pigments plays a vital role in their application and NIR reflectance needs to be strong enough for various harsh working conditions. The chemical stability of the nano-pigments was examined by mixing the pigments with H_2O, 5% HNO_3, HCl, and NaOH solution thoroughly using a magnetic stirrer for 20 min. Then, the soaked samples were filtered and washed several times using a distilled water in an centrifuge to remove the acid content. Finally, the resultant pigment was oven-dried by maintaining at 70 °C for 5 h. Subsequently, the CIE color coordinates, chroma, and H° values of the acid/alkali treated nano-pigments were examined and the values are tabulated in Table 2. In addition, the color difference (ΔE^*) of the nano-pigments after being treated with acid/alkali solution was also estimated and is listed in Table 2. As shown in the table, the estimated ΔE^* for the LWO material exhibits an acceptable color difference in the H_2O and NaOH; whereas the HNO_3 and HCl treated samples show diminished chemical stability, since ΔE^* values were greater than the permitted limit ($\Delta E^* \geq 5$). Similarly, the LWZO nano-pigment also follows a similar trend by exhibiting good chemical stability for alkali solutions, nevertheless, revealing larger ΔE^* values for acids (HNO_3 and HCl). Concurrently, the LWCO, LWCuO, and LWFO nano-pigments have excellent chemical stability with $\Delta E^* \leq 5$,

Table 2 The chroma parameters and color difference (ΔE^*) values of the prepared nano pigments after acid/alkali treatment.

		CIE $L^*a^*b^*$					
Pigments	Treatment	L^*	a^*	b^*	C^*	H^*	ΔE^*
LWO	Without	91.84	−3.6	6.9	7.79	117.6	—
	H_2O	92.63	−3.29	6.82	7.57	115.8	0.85
	HNO_3	83.13	−1.52	38.7	38.73	92.25	33.04
	HCl	85.34	−6.19	36.8	37.32	99.54	30.71
	NaOH	93.55	−2.85	6.86	7.43	112.6	1.87
LWCuO	Without	80.87	−3.29	24.39	24.61	97.67	—
	H_2O	81.63	−3.32	23.95	24.18	97.9	0.88
	HNO_3	82.96	−3.99	25.55	25.86	98.88	2.49
	HCl	81.9	−3.49	27.14	27.37	97.33	2.94
	NaOH	84.43	−3.27	20.29	20.55	99.16	5.43
LWCO	Without	62.01	−0.69	−2.57	2.66	254.9	—
	H_2O	63.14	−0.8	−2.49	2.62	252.2	1.14
	HNO_3	65.3	−0.87	−1.91	2.1	245.5	3.36
	HCl	67.34	−2.55	1.9	3.18	143.3	7.20
	NaOH	66.95	−1.17	−2.48	2.74	244.7	4.96
LWZO	Without	94.42	−2.57	7.39	7.83	109.2	—
	H_2O	94.58	−2.5	7.04	7.47	109.6	0.39
	HNO_3	91.78	−6.05	22.3	23.1	105.2	15.54
	HCl	91.32	−5.52	17.07	17.94	107.9	10.58
	NaOH	93.6	−2.48	7.63	8.02	108	0.86
LWFO	Without	62.77	19.34	19.79	27.67	45.66	—
	H_2O	63.09	19.49	19.62	27.66	45.19	0.39
	HNO_3	62.47	19.92	20.39	28.51	45.66	0.89
	HCl	63.6	19	20.19	27.72	46.74	0.98
	NaOH	61.9	19.39	19.15	27.25	44.64	1.08

indicating their outstanding alkali/acid resistance. This feature makes them excellent materials for cooling applications. Interestingly, the nano-pigments underwent high-temperature calcination during their preparation (1000 °C for 6 h), implying that they can sustain high temperatures without altering their chromatic properties. In addition, the photostability of the prepared nano-pigments was examined by continuously irradiating IR light for 48 h. Later, the CIE color coordinates, chroma, $H°$, and ΔE^* values of the pigments after continuous irradiation of the light were estimated and are given

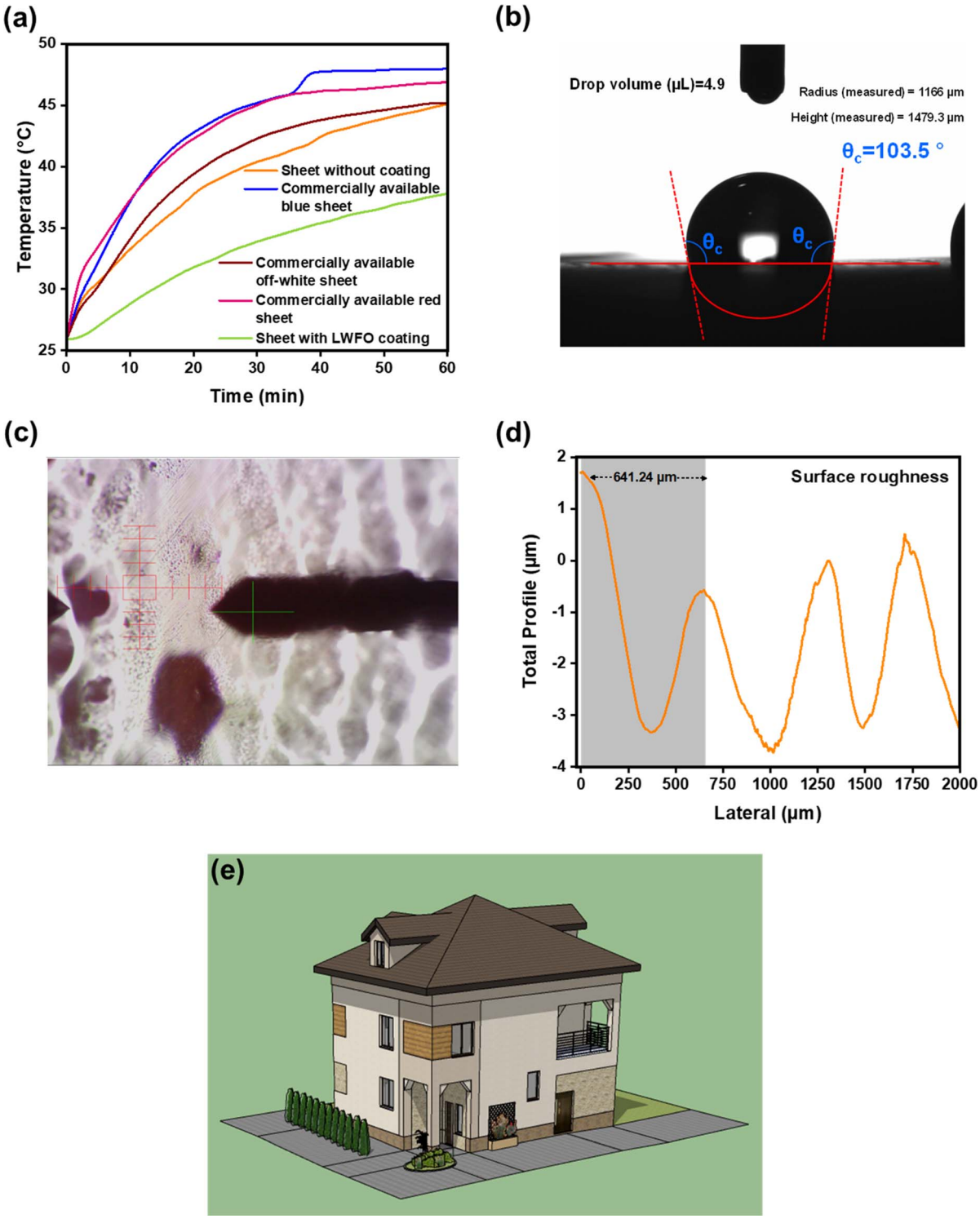

Fig. 8 (a) The interior temperature of the house model with different roofing materials. (b) The water contact angle of the LWFO pigment-coated aluminum sheet, (c) and (d) the profilometer trace of surface roughness analysis test of the coated sheet, and (e) the mid-rise apartment model established by *OpenStudio* software.

in Table S3.† The calculated values clearly show that the ΔE^* values of the pigments by considering before and after irradiation were found to be in the acceptable range of difference ($\Delta E^* \leq 5$). The aforementioned results demonstrate that the prepared nano-pigments exhibit excellent chemical, thermal, and photostability properties, which show their potential as an excellent candidature for cooling applications.

The thermal conductivity study of the synthesized nano-pigments was examined at room temperature. The thermal conductivity of the prepared pigments was found to be 0.07–0.08 W m^{-1} K^{-1}. The prepared pigments revealed low thermal conductivity as compared to conventional roofing materials. For instance, Xu *et al.*[70] studied the thermal conductivity of the conventionally used concrete mortar and found it to be 0.58 W m^{-1} K^{-1}. Chung *et al.*[71] also investigated the thermal conductivity of the wood-plastic composite (WPC) which was shown to be 0.53 W m^{-1} K^{-1}; the thermal conductivity of bare concrete is 2.29 W m^{-1} K^{-1}. Interestingly, the prepared LWFO nano-pigment showcased excellent NIR reflectance, low thermal conductivity, chemical, thermal, and photostable properties along with better color perception as compared to LWCO, LWCuO, and LWZO nano-pigments. After these careful evaluations, LWFO was considered to be the best-performing pigment among others for UHI applications. Hence, a comparison study of a thermal shielding test using the plywood house model with the LWFO nano-pigment-coated aluminum sheet and commercially available sheets as a roof was performed. As given in the experimental section, a plywood house model with LWFO nano-pigment coated aluminum sheet and commercially available sheets (bare sheet, blue sheet, off-white sheet, and red sheet) were placed under an IR lamp positioned 40 cm above the roof as well as temperature sensors were provided to record the interior temperature of the model (Fig. S5†). Subsequently, time-dependent temperature measurements were noted, and the corresponding plots are depicted in Fig. 8(a). As shown in the figure, the interior temperature of the models increased with increasing time up to 40 min, and a steady temperature was reached after 1 hour of IR irradiation in pigment-coated sheet and commercial sheet-based models. Interestingly, a similar trend was also noticed in other comparison investigations; the temperature difference (Δt) between the nano-pigment coated and the bare aluminum sheet was found to be −7 °C, indicating that the coated sample supports a 7 °C cooler interior than the bare aluminum sheet roofing interior. The Δt values between coated sheets with commercially available blue off-white, and red sheets were ∼−10 °C, −7 °C, and −8 °C, respectively. These results demonstrated that the interior of the LWFO pigment-coated sheet delivers a cooler atmosphere as compared to the conventional sheet interior. The aforementioned results endorse the applicability of the prepared pigment with excellent NIR reflectance for passive daytime radiative cooling applications. Furthermore, to investigate the wettability of the nano-pigment-coated surface, the WCA was measured and shown in Fig. 8(b). The microliter (μl) drop WCA of the coated surface was estimated and found to be ∼103.5°. The obtained result demonstrated that the coated surface is hydrophobic and becomes water-repellent. Fig. S6† demonstrates the comparison of WCA of various pigment coatings with a prepared LWFO coating. It is noteworthy that Fatah *et al.*[72] studied the WCA of the blue-pigmented coated surface and found it to be ∼107.7°. Further, the blue pigment with ZnO nanoparticles coated surface exhibits a WCA of about 114.3°, which indicates its hydrophobicity. However, the surface-modified corresponding pigment by an antifouling agent showcases the superhydrophobic nature with the WCA of ∼145.4°. The antifouling agent covered the porous structure on the surface and reduced the surface energy, resulting in a surface that resembles the natural superhydrophobic lotus leaf. Similarly, Wang *et al.*[73] also investigated the hydrophobic modification of $ZnTiO_3$-based thermal insulation functional composite coatings using silicone resin. The WCAs of $ZnTiO_3$ and silicone were 25° and 102°. The very small WCA of bare $ZnTiO_3$ signifies the hydrophilic surface of the particles. However, $ZnTiO_3$ and silicone-based composites (with different % of $ZnTiO_3$) have improved the WCA up to ∼122° (Fig. S5†). The results confirm that the surface of $ZnTiO_3$ particles have been successfully converted from hydrophilic to hydrophobic. However, cellulose nanocrystals and their dye showcase WCAs of ∼49.75 and 62.13°, respectively, with a hydrophilic surface nature.[74] In comparison, the prepared LWFO nano-pigment coated surface demonstrated a hydrophobic nature without any surface modification strategy and tended to avoid water absorption and adherence on the surface. Hence, the hydrophobic nature of the coating protects the coating from contamination to maintain a stable cooling performance. The roughness of the nano-pigment coating on the aluminum sheet was investigated by the surface profile test and is given in Fig. 8(c and d). From the obtained plot, the mean roughness of the pigment film was found to be lower than 5 μm. The uniform roughness and excellent water-repellent property of the prepared cooling LWFO nano-pigment demonstrated its applicability in conventional cool roofing systems to mitigate UHI.

The efficient energy-saving ability of the designed nano-pigments in actual buildings by circumventing solar energy conduction inside a building was further evaluated and quantified using *EnergyPlus* software *via* simulating energy consumption. Bengaluru city, Karnataka, India was selected to simulate energy consumption since it has the fourth most populous urban agglomeration in India, a tropical savanna climate with occasional heatwaves, and it reached a maximum temperature of around 36.5 °C during summer 2023. The *openstudio* software was used to design a mid-rise apartment (Fig. 8(e)) with a total area of 268 m^2 provided with an HVAC system for cooling and heating and a total indoor occupant density of 0.1670 people per m^2. The heating and cooling temperatures were fixed at 18 °C and 26 °C, respectively. After simulation, the energy consumption of the HVAC system was analyzed and tabulated in Table S4.† As witnessed from the table, the total electricity required for cooling in a year of the designed building coated with the best performing LWFO nano-pigment is found to be 32.45 kW h m^{-2}, and the electricity cost per month was assessed to be $162.25. The obtained results were compared with conventional exterior coatings, such as cement and pearlescent pigment; demonstrating the LWFO

pigment coating can reduce electricity utilization by up to 17.54 kW h m^{-2} and save costs of $87.7 per month. From these results, we can conclude that the synthesized various chromophores doped-LWO cooling pigments with high reflectance are suitable candidates as a thermal passive radiative cooling material for external coating to alleviate UHI effects.

4. Conclusions

In summary, a series of various chromophore-doped $La_2W_{1.86}M_{0.14}O_9$ (M = Co, Cu, Zn, and Fe) radiative cooling nano-pigments were rationally designed and synthesized by the SC route. Morphological studies of the nano-pigments show irregular ribbons, dumbbells, and flaky-type morphologies with large agglomeration and voids, which are obvious morphologies in the SC route-derived samples. The absorption spectra of the established pigments have revealed both the metal-to-metal charge transfer as well as d–d transitions simultaneously, which results in the possibility of obtaining various colors. The E_g values of the prepared nano-pigments were estimated and calculated to be around 2.83–3.78 eV. Indeed, the prepared pigments have a large quantity of solar irradiance spectral concealment, implying their advantage as coating materials to reflect solar radiations. The designed cooling pigments show excellent thermal, chemical, and photo stabilities, which endorse their adaptivity to several provision conditions. In addition, the wettability and surface roughness profile test results of the nano-pigment-coated surface exhibit a uniform coating with a water contact angle of ~103.5°, demonstrating that the coated surface makes the surface hydrophobic and water-repellent. Further, it can be protected from external contamination to maintain a stable cooling performance. These results established in this report will be beneficial for endorsing the development of efficient high NIR reflectance passive radiative cooling pigments, which could be pursued as an energy-efficient and economical solution for mitigating urban heat islands effects and contributing to boosting energy sustainability.

Data availability

The data supporting this article have been included as part of the ESI.†

Conflicts of interest

There are no conflicts to declare.

Acknowledgements

The author G. P. D. acknowledges graduate students Deependra Singh Rao, Goutham C, and Shreya Gaupale for their significant contributions and is also grateful to the management of M. S. Ramaiah University of Applied Sciences, Bengaluru for sanctioning seed money-funded project [Ref: RUAS/DSR/SEED MONEY/2022/1012].

References

1 W. Schulz, J. Fraillon, G. Agrusti, J. Ainley, B. Losito, and T. Friedman, *Becoming Citizens in a Changing World: IEA International Civic and Citizenship Education Study 2016 International Report*, 2018, vol. 1, pp. 1–243.
2 A. Kundu, *Human Development Research Paper*, 2009, vol. 16, pp. 1–55.
3 A. Banerjee, *Rev. World Econ.*, 2015, **152**, 3–17.
4 M. Santamouris and K. Vasilakopoulou, *E.-Prime – Adv. Electr. Eng. Electron. and Energy*, 2021, **1**, 100002.
5 Y. H. Yau and S. Hasbi, *Renewable Sustainable Energy Rev.*, 2013, **18**, 430–441.
6 E. Scoccimarro, O. Cattaneo, S. Gualdi, F. Mattion, A. Bizeul, A. M. Risquez and R. Quadrelli, *Commun. Earth Environ.*, 2023, **4**, 208.
7 B. Bandyopadhyay and M. Banerjee, *Solar Compass*, 2022, **2**, 100025.
8 U.N.E. Programme, *2022 Global Status Report for Buildings and Construction: towards a Zero Emission, Efficient and Resilient Buildings and Construction Sector*, 2022.
9 A. I. Osman, L. Chen, M. Yang, G. Msigwa, M. Farghali, S. Fawzy, D. W. Rooney and P. S. Yap, *Environ. Chem. Lett.*, 2023, **21**, 741–764.
10 R. Yang, A. Han, M. Ye, X. Chen and L. Yuan, *Sol. Energy Mater. Sol. Cells*, 2017, **160**, 307–318.
11 S. Hanauer, I. Massiot, A. Mlayah, F. Carcenac, J. B. Doucet, S. Beldjoudi, I. Faniayeu and A. Dmitriev, *ACS Appl. Energy Mater.*, 2023, **6**, 2128–2133.
12 J. Lizana, M. de-Borja-Torrejon, A. Barrios-Padura, T. Auer and R. Chacartegui, *Appl. Energy*, 2019, **254**, 113658.
13 M. Saffari, A. de Gracia, S. Ushak and L. F. Cabeza, *Renewable Sustainable Energy Rev.*, 2017, **80**, 1239–1255.
14 H. Akeiber, P. Nejat, M. Z. A. Majid, M. A. Wahid, F. Jomehzadeh, I. Zeynali Famileh, J. K. Calautit, B. R. Hughes and S. A. Zaki, *Renewable Sustainable Energy Rev.*, 2016, **60**, 1470–1497.
15 S. Jose, D. Joshy, S. B. Narendranath and P. Periyat, *Sol. Energy Mater. Sol. Cells*, 2019, **194**, 7–27.
16 S. Wu, Y. Cao, Y. Li and W. Sun, *Adv. Opt. Mater.*, 2023, **11**, 2202163.
17 W. Zhou, J. Ye, Z. Liu, L. Wang, L. Chen, S. Zhuo, Y. Liu and W. Chen, *Inorg. Chem.*, 2022, **61**, 693–699.
18 S. Jose, A. Prakash, S. Laha, S. Natarajan and M. L. Reddy, *Dyes Pigm.*, 2014, **107**, 118–126.
19 F. Song, Y. Li, Y. Yu, Z. Shen, Z. Wang and X. Li, *J. Solid State Chem.*, 2020, **282**, 121110.
20 B. Huang, Y. Xiao, C. Huang, J. Chen and X. Sun, *Dyes Pigm.*, 2017, **147**, 225–233.
21 A. Han, M. Ye, M. Zhao, J. Liao and T. Wu, *Dyes Pigm.*, 2013, **99**, 527–530.
22 J. Zou, Y. Chen and P. Zhang, *Ceram. Int.*, 2021, **47**, 12661–12666.
23 W. Zhou, J. Ye, S. Zhuo, D. Yu, P. Fang, R. Peng, Y. Liu and W. Chen, *J. Alloys Compd.*, 2022, **896**, 162883.

24 J. Wang, A. Han, M. Ye, C. Chen, X. Chen and X. Zhu, *ACS Sustain. Chem. Eng.*, 2021, **9**, 16328–16337.
25 M. Fortuño-Morte, P. Serna-Gallén, H. Beltrán-Mir and E. Cordoncillo, *J. Materiomics*, 2021, **7**, 1061–1073.
26 Y. Li, Y. Ma, W. liu, Z. Wang, H. Liu, X. Wang, H. Wei, S. Zeng, N. Yi and G. J. Cheng, *Sol. Energy*, 2021, **226**, 180–191.
27 C. Chen, A. Han, J. Wang, Y. Su and M. Ye, *Sol. Energy*, 2023, **262**, 111857.
28 Y. Xiao, L. Feng, B. Huang, J. Chen, W. Xie and X. Sun, *Ceram. Int.*, 2021, **47**, 29856–29863.
29 J. Zou and P. Zhang, *Ceram. Int.*, 2020, **46**, 3490–3497.
30 M. Bai, W. Li, Y. Hong, S. Wang, Y. Wang and Q. Chang, *Sol. Energy*, 2022, **234**, 240–250.
31 M. Zhang, L. Feng, Z. Zeng, Y. Yang and X. Sun, *ACS Sustain. Chem. Eng.*, 2022, **10**, 13877–13886.
32 X. Wang, X. Feng, C. Gong, M. Sun, C. Wang, Q. Wang and J. G. Li, *J. Asian Ceram. Soc.*, 2021, **9**, 1419–1428.
33 P. Urbanowicz, M. Piatkowska, B. Sawicki, T. Groń, Z. Kukuła and E. Tomaszewicz, *J. Eur. Ceram. Soc.*, 2015, **35**, 4189–4193.
34 Y. Zhu, Y. Liu, G. Tan, W. Liu, H. Ren, D. H. Liu, S. Bai, R. Wang and S. Ye, *Ceram. Int.*, 2020, **46**, 18184–18192.
35 Q. Cheng, F. Ren, Q. Lin, H. Tong and X. Miao, *J. Alloys Compd.*, 2019, **772**, 905–911.
36 K. Nassau, The origins of color in minerals, *Am. Mineral.*, 1978, **63**, 219–229.
37 M. A. Subramanian and J. Li, *Mater. Today Adv.*, 2022, **16**, 100323.
38 H. Shirai, S. Tamura and N. Imanaka, *Ceram. Int.*, 2022, **48**, 8729–8732.
39 J. de O. Primo, K. W. Borth, D. C. Peron, V. de C. Teixeira, D. Galante, C. Bittencourt and F. J. Anaissi, *J. Alloys Compd.*, 2019, **780**, 17–24.
40 J. Zheng, Z. Li, Y. Zheng, W. Zhao, F. Tan, F. Yang, H. Chen and L. Xue, *Ceram. Int.*, 2023, **49**, 558–564.
41 C. Darshan, A. Arjun, H. B. Premkumar, G. P. Darshan, S. C. Sharma and H. Nagabhushana, *Mater. Today Sustain.*, 2023, **24**, 100594.
42 F. Femila Komahal, H. Nagabhushana, G. P. Darshan and B. Daruka Prasad, *Arabian J. Chem.*, 2020, **13**, 580–594.
43 M. Sakata and M. J. Cooper, *J. Appl. Crystallogr.*, 1979, **12**, 554–563.
44 D. Marrero-López, J. Peña-Martínez, J. C. Ruiz-Morales and P. Núñez, *J. Solid State Chem.*, 2008, **181**, 253–262.
45 G. P. Darshan, A. Arjun, H. B. Premkumar, G. Tamilarasu, S. C. Sharma, H. Nagabhushana and S. O. Manjunatha, *J. Alloys Compd.*, 2023, **960**, 170662.
46 A. Varma, A. S. Mukasyan, A. S. Rogachev and K. V. Manukyan, *Chem. Rev.*, 2016, **116**(23), 14493–14586.
47 A. G. Merzhanov, *J. Mater. Chem.*, 2004, **14**, 1779–1786.
48 P. Makuła, M. Pacia and W. Macyk, *J. Phys. Chem. Lett.*, 2018, **9**(23), 6814–6817.
49 H. Najafi-Ashtiani, A. Bahari, S. Gholipour and S. Hoseinzadeh, *J. Appl. Phys.*, 2018, **124**, 1–9.
50 M.-Y. Li, S.-S. Wen, S.-Q. Jin, R. Hatel and M. Baitoul, *J. Phys.: Conf. Ser.*, 2019, **1292**, 012014.
51 E. C. Samano, G. Soto, J. Valenzuela and L. Cota, *J. Vac. Sci. Technol., A*, 1997, **15**, 2585–2591.
52 Y. P. He, Y. M. Miao, C. R. Li, S. Q. Wang, L. Cao, S. S. Xie, G. Z. Yang, B. S. Zou and C. Burda, *Phys. Rev. B: Condens. Matter*, 2005, **71**, 125411.
53 Y. Wang and R. K. Li, *Opt. Mater.*, 2010, **32**, 1313–1316.
54 S. L. Reddy, T. Endo and G. S. Reddy, *Adv. Aspects Spectrosc.*, 2012, 4–48.
55 L. I. Granone, K. Nikitin, A. Emeline, R. Dillert and D. W. Bahnemann, *Catalysts*, 2019, **9**, 434.
56 N. Sinha and O. S. Wenger, *J. Am. Chem. Soc.*, 2023, **145**, 4903–4920.
57 S. R. Qiu, B. C. Wood, P. R. Ehrmann, S. G. Demos, P. E. Miller, K. I. Schaffers, T. I. Suratwala and R. K. Brow, *Phys. Chem. Chem. Phys.*, 2015, **17**, 18913–18923.
58 R. Glaum, K. Gerber, M. Schulz-Dobrick, M. Herklotz, F. Scheiba and H. Ehrenberg, *J. Solid State Chem.*, 2012, **188**, 26–31.
59 S. Kumar, P. K. Pandey, N. Sinha, S. Chaudhari and S. Sharma, *J. Phys. Sci.*, 2018, **29**, 1–11.
60 H. B. Premkumar, A. Arjun, M. V. Sharvani, S. C. Sharma, H. Nagabhushana and G. P. Darshan, *Inorg. Chem. Commun.*, 2023, **158**, 111637.
61 D. Joshy, C. P. Jijil, S. Jose, Y. A. Ismail and P. Periyat, *Mater. Adv.*, 2022, **3**, 6584.
62 S. G. Menon and H. C. Swart, *J. Alloys Compd.*, 2020, **819**, 152991.
63 Ju L. Hyeon, K. Y. Jung and Y.-S. Kim, *RSC Adv.*, 2021, **11**, 16834–16840.
64 S. Zeng, Z. Wang, Y. Ma, X. Wang and H. Liu, *J. Alloys Compd.*, 2022, **899**, 163244.
65 L. Cai, X. Wu, Q. Gao and Y. Fan, *Dyes Pigm.*, 2018, **156**, 33–38.
66 J. Liu, J. Luo, F. Shi, S. Liu, C. Fan, Q. Xu and G. Shao, *J. Solid State Chem.*, 2015, **221**, 255–262.
67 Z. Cheng, F. Wang, H. Wang, H. Liang and L. Ma, *Int. J. Therm. Sci.*, 2019, **140**, 358–367.
68 A. Bin Yousaf, M. Imran, M. Farooq and P. Kasak, *Sci. Rep.*, 2018, **8**, 4354.
69 L. Li, P. Ma, S. Hussain, L. Jia, D. Lin, X. Yin, Y. Lin, Z. Cheng and L. Wang, *Sustainable Energy Fuels*, 2019, **3**, 1749–1756.
70 S. Xu, J. Liu and Q. Zeng, *Mater. Des.*, 2018, **157**, 105–118.
71 M. H. Chung and J. C. Park, *Energies*, 2017, **10**(2), 195.
72 S. K. Fatah, M. Khajeh Aminian and M. Bahamirian, *Ceram. Int.*, 2022, **48**, 21913–21925.
73 S. Wang, J. Wang, S. Wen, H. Li, C. Xie, S. Li and D. Mei, *RSC Adv.*, 2023, **13**, 6065.
74 L. Kang, P. Chen, B. Wang, J. Jia, J. Li, J. Zeng, Z. Cheng, W. Gao, J. Xu and K. Chen, *Cellulose*, 2020, **27**, 905–913.

